Materials Science and Engineering C 59 (2016) 324–332

Contents lists available at ScienceDirect

Materials Science and Engineering C

journal homepage: www.elsevier.com/locate/msec

Aptamer-conjugated, fluorescent gold nanorods as potential cancer theradiagnostic agents

Maria Elena Gallina [a,*], Yu Zhou [b], Christopher J. Johnson [b], David Harris-Birtill [a], Mohan Singh [a], Hailin Zhao [c], Daqing Ma [c], Tony Cass [b], Daniel S. Elson [a]

[a] Hamlyn Centre for Robotic Surgery, Institute of Global Health Innovation and Department of Surgery and Cancer, Imperial College London, UK
[b] Department of Chemistry, Institute of Biomedical Engineering and Chemical Biology Centre, Imperial College London, UK
[c] Department of Surgery and Cancer, Imperial College London, UK

ARTICLE INFO

Article history:
Received 12 March 2015
Received in revised form 21 September 2015
Accepted 28 September 2015
Available online 3 October 2015

Keywords:
Gold nanorods
Aptamer
Targeted cancer labelling
Fluorescence microscopy
Photothermal therapy

ABSTRACT

GNRs are emerging as a new class of probes for theradiagnostic applications thanks to their unique optical properties. However, the achievement of proper nanoconstructs requires the synthesis of highly pure GNRs with well-defined aspect ratio (AR), in addition to extensive surface chemistry modification to provide them with active targeting and, possibly, multifunctionality.

In this work, we refined the method of the seed mediated growth and developed a robust procedure for the fabrication of GNRs with specific AR. We also revealed and characterized unexplored aging phenomena that follow the synthesis and consistently alter GNRs' final AR. Such advances appreciably improved the feasibility of GNRs fabrication and offered useful insights on the growth mechanism.

We next produced fluorescent, biocompatible, aptamer-conjugated GNRs by performing ligand exchange followed by bioconjugation to anti-cancer oligonucleotide AS1411. *In vitro* studies showed that our nanoconstructs selectively target cancer cells while showing negligible cytotoxicity. As a result, our aptamer-conjugated GNRs constitute ideal cancer-selective multifunctional probes and promising candidates as photothermal therapy agents.

1. Introduction

The application of nanoparticles in the biomedical field achieved a position of increasing significance over the last twenty years [1]. Among the range of nanomaterials, gold nanoparticles (GNPs) are suited to an extensive array of medical applications. This versatility is due to the high modularity of their optical properties. The electrons belonging to the conduction band of GNPs undergo collective surface oscillations, called surface plasmon resonance (SPR), which originate high absorption and scattering cross sections. The resonance frequency and the ratio between absorption and scattering contributions strongly depend on the size and the shape of the nanoparticles [2]. Applying different synthetic strategies can modulate these properties, indeed, in the last ten years, GNPs' design and composition have been optimized on the basis of the desired applications. Currently, GNPs are used as contrast agents in several imaging techniques, including two-photon luminescence microscopy [3,4], optical coherence tomography [5] and photoacoustic tomography [6,7]. They are also employed as probes for cancer diagnosis, optically guided tumour surgery, and lymph node mapping applications [7–9]. Furthermore, in the past decade, GNPs have been used as cancer treatment agents [10–12] for diagnostics and therapeutics at the same time [13–15]. In oncology, one of most advantageous properties of GNPs is the elevated conversion rate of absorbed radiations into heat. Hirsch and co-workers showed that the heat released by irradiated GNPs can been used to ablate tumour sites [16], paving the way for an innovative type of cancer treatment, today known as photothermal therapy (PTT). PTT is based on the accumulation of GNPs in the cancer site followed by exposition to electromagnetic emissions such as near infrared laser light. These radiations are capable of exciting GNPs [16] without being absorbed by nanoparticles-free tissues. The local temperature rise caused by the presence of GNPs is supposed to damage the membrane of cancer cells promoting tumour death by apoptosis. Preliminary studies showed that PTT, used in combination with chemo- [12,17] or photodynamic-therapy [11], enhances the tumour response, inasmuch that it may also constitute an alternative approach in chemotherapy-resistant cancers [18].

Among the variety of GNPs, the employment of gold nanorods (GNRs) for PTT presents several advantages: they have small size, narrow spectra bandwidths (see Fig. 1a) and high absorption cross sections [1]. Furthermore, while the transverse surface plasmon resonance

* Corresponding author.
E-mail address: m.gallina@imperial.ac.uk (M.E. Gallina).

http://dx.doi.org/10.1016/j.msec.2015.09.101

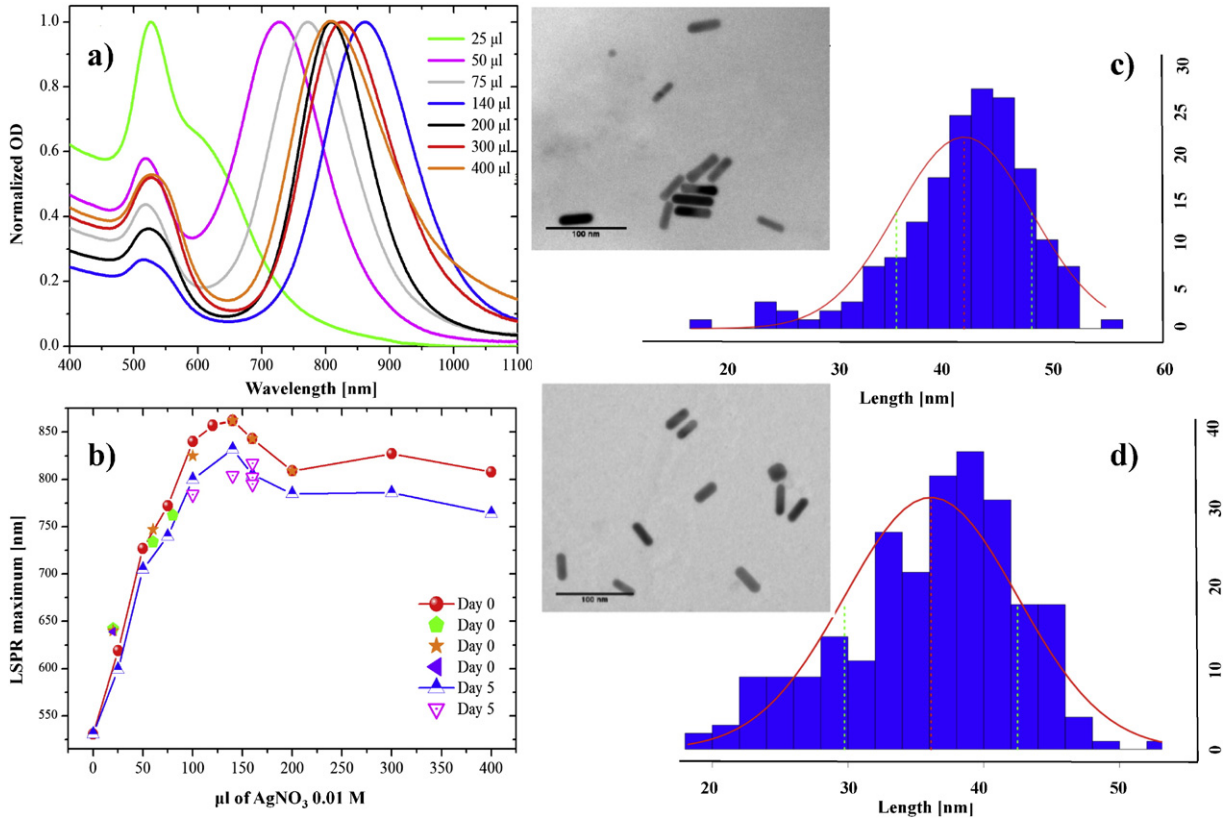

Fig. 1. a) Optical density spectra of CTAB-coated GNRs synthesized with different volumes of $AgNO_3$ 0.01 M recorded on day 0 after partial CTAB removal by single centrifugation. b) Wavelength of LSPR maximum after partial CTAB removal as a function of $AgNO_3$ content on day 0 (red dots, orange stars, purple triangles and green pentagons account for different experiments conducted in the same conditions) and day 5 (blue and magenta-edged triangles). Length distributions of GNRs synthesized using 100 µl of $AgNO_3$ 0.01 M by TEM analysis on day 0 (c) and day 5 (d). Red lines represent the best-fitting Gaussian distribution of frequency histograms. Average values are indicated by red dashed lines and correspond to 43 (±1.5) nm at day 0 and 36 (±1.4) nm at day 5. Green dashed lines represent the average lengths plus and minus the corresponding standard deviation. Insets: representative TEM images of GNRs synthesized with 100 µl of $AgNO_3$ on day 0 (c) and day 5 (d).

(TSPR) is centred around 520 nm, causing the typical red appearance, the longitudinal surface plasmon resonance (LSPR) can be finely tuned in the near infrared region (NIR) by adjusting the aspect ratio (AR) (length/width) [19].

Despite GNRs' outstanding optical properties, their synthesis and functionalization is not a trivial task. First of all, the mechanism of the seed-mediated growth [20,21], the most common preparation route of GNRs, is poorly comprehended [22]. The lack of a molecular level understanding of the fabrication mechanism leads to major difficulties in controlling the reproducibility and poses questions on the interplay of different variables determining the shape and the AR. Moreover, the occurrence of aging phenomena [23] still needs adequate characterization, and further compromises the fine control of the size and the structure of GNRs. Secondly, GNRs obtained by seed-mediated growth are capped by a double layer of cetyl trimethyl ammonium bromide (CTAB), a surfactant that plays a critical role in driving the seeds' growth towards the cylindrical shape. CTAB is highly cytotoxic and needs to be removed for biological applications [24], however its complete elimination is difficult to achieve and can cause irreversible aggregation. Several methods have been proposed for the substitution of CTAB with alkanethiols, polyethylene glycol (PEG) derivatives or other macromolecules [25–27]. So far, functionalization with thiol-PEG is regarded as one of the most effective ways to achieve stable, water-soluble GNRs with good biocompatibility [7]. *In vivo* studies showed that PEG-functionalized GNPs (PEG-GNPs) have longer circulation time [28] and can accumulate on cancer sites by enhanced permeability and retention (EPR) effect [29].

Specificity of tumour accumulation and binding can be improved by functionalization of PEG-GNRs with cancer targeting agents, such as antibodies or small peptides [30]. Privileged uptake of GNRs conjugated to cancer-specific antibodies has been observed *in vitro* [31,32,13], but statistical difference *in vivo* between targeted and non-targeted GNRs has not been verified yet. One possible alternative to antibodies was recently found in the discovery of aptamers: short DNA or RNA single-strands capable of forming unique three-dimensional structures that bind specific molecular targets. This new class of recognition system offers significant advantages: small size, low immunogenicity and higher affinity. They also provide synthetic accessibility at lower costs, improved chemical stability, and flexible design with possibility of further functionalization [33].

In this work, we designed and produced fluorescent, biocompatible, aptamer-conjugated GNRs. These nanoconstructs can be used as multifunctional probes for cancer imaging and, possibly, PTT. GNRs with specific AR were obtained by refinement of the synthesis method developed by Murphy et al. [22]. Aging phenomena that altered the final AR were characterized by TEM and spectrophotometric analysis. Once GNRs were fully aged, the extinction coefficient at the LSPR maximum was estimated by combining spectrophotometric data with optical, microscopy-based concentration measurements via nanoparticles tracking. We then successfully developed a facile conjugation method for obtaining PEG-GNRs covalently bound to a fluorescent version of aptamer AS1411 [34]. AS1411 is an anti-cancer oligonucleotide that can be specifically internalized by cancer cells. The uptake mechanism has been described as nucleolin-driven endocytosis [35], nucleolin being a receptor overexpressed in the membrane and the cytoplasm of some tumour cells. We used fluorescence microscopy to verify that only cancer cells internalized AS1411-GNR conjugates (AC-GNRs). Labelling of cancer cells by AC-GNRs was also confirmed by flow cytometry experiments.

Cytotoxicity tests revealed that AC-GNRs have negligible poisonousness under the conditions used for fluorescence labelling.

Obtained results open the way to the usage of our biocompatible, fluorescent, aptamer conjugated GNRs as multifunctional, cancer-specific imaging probes. These novel nanoconstructs are good candidates for cancer diagnostic, and for potential PTT treatments; our laboratory is planning to investigate the latter point in future studies.

2. Materials and methods

2.1. Materials

CTAB was purchased from Calbiochem, silver nitrate ($AgNO_3$), gold(III) chloride trihydrate ($HAuCl_4 \cdot 3H_2O$), sodium borohydride ($NaBH_4$), L-ascorbic acid (AA), N-(3-Dimethylaminopropyl)-N′-ethylcarbodiimide hydrochloride (EDC), N-Hydroxysuccinimide (NHS) and Potassium Carbonate (K_2CO_3) were purchased from Sigma Aldrich. Heterobifunctional thiol carboxyl PEG (HS–$(O–CH_2–CH_2)_n$–$(CH_2)_2$–COOH, MW = 2 kDa) and Cy5 amine PEG (Cy5–CONH–$(O–CH_2–CH_2)_n$–$(CH_2)_2$–NH_2, MW = 5 kDa) were purchased from Nanocs, and custom-modified AS1411 ($H_2N–C_6H_{12}$–5′-TTT GGT GGTGGTGGT TGT GGT GGTGGT GG-3′–C_3H_6–Cy5) was ordered from Integrated DNA Technologies. Calcein AM ($C_{46}H_{46}N_2O_{23}$) assay was purchased from Trevigen, while DNAse/RNAse free distilled water, phosphate buffered saline (PBS) solution, Dulbecco's Modified Eagle Medium (DMEM), fetal bovin serum (FBS), trypsin and ethylenediamine tetra acetic acid (EDTA) solution and L-glutamine were obtained from Life Technologies. Purified water (18.2 MΩ cm) was produced by a Millipore water purification system.

2.2. Synthesis of GNRs via seed-mediated growth

CTAB-capped GNRs were fabricated using a modified version of the seed mediated growth method reported by Murphy et al. [22]. High purity water was used at all steps. The seed solution was produced by adding 600 μl of ice-cold 0.01 M $NaBH_4$ to 10.0 ml of CTAB aqueous solution 0.1 M containing $HAuCl_4$ 2.5 10^{-4} M for 7 min under slow agitation. Afterwards, the stirring was stopped and the mixture was kept at 30 °C for at least 1 h. The growth solution was prepared by mixing 160 μl of $AgNO_3$ 0.01 M to 9.5 ml of CTAB 0.1 M. The addition of 500 μl of $HAuCl_4$ 0.01 M was followed by that of 55 μl of AA 0.1 M. 12 μl of the seed solution were then added to the mixture at 30 °C. After it was left in the dark for 1 h, CTAB excess was removed by centrifugation at 8500 rpm and 30 °C for 15 min.

2.3. Pegylation and bioconjugation

Pegylation of GNRs was performed once the amount of CTAB was reduced to a minimum by two centrifugation steps. Further purification attempts failed owing to irreversible aggregation of GNRs. After sonication, 5 ml of concentrated CTAB-capped GNRs/water solution were mixed with equal volumes of K_2CO_3 2 mM and HS–$(O–CH_2–CH_2)_n$–$(CH_2)_2$–COOH aqueous solutions. The mixture was kept in the dark under sonication for 3 h and left overnight on a rotary shaker. It was then diluted and centrifuged at 8500 rpm and 30 °C for 15 min; the precipitate was collected and re-dissolved in PBS. The sample was dialyzed against PBS for 2 days (MWCO = 8–10 kDa) (Spectrum Laboratories, USA) and kept in the dark at 4 °C. Size and ζ-potential measurements were performed before and after the ligand exchange to confirm the functionalization of GNRs with thiol carboxyl PEG (COOH–PEG–GNRs, see Scheme 1). In order to win the competition with CTAB, large excess (*ca.* eight times) of thiol carboxyl PEG with respect to the expected number of PEG chains binding GNRs [36] was applied.

GNRs were conjugated to custom-modified AS1411 (H_2N–AS1411–Cy5, see Scheme 1) by EDC/NHS catalysed reaction between carboxylate-functionalized GNRs and amine-containing aptamers. 500 μl of COOH–PEG–GNRs PBS solution with OD_{max} = 0.3 were mixed with 50 mM solutions of EDC and NHS under vortex. The typical molar ratio between EDC and NHS was 1:2. The reaction was left to proceed at ambient temperature for 20 min under continuous agitation; it was then diluted and centrifuged at 8500 rpm for 15 min. The precipitate was collected and, once redissolved in 500 μl of DNAse/RNAse free water, it was mixed with 0.1 mM H_2N–AS1411–Cy5 and left reacting for 4 h in a rotary shaker. After centrifugation, the precipitate was dissolved in DNAse/RNAse free water and dialyzed for 2 days (MWCO = 12–14 kDa) (Spectrum Laboratories, USA) in order to purify the product from unreacted H_2N–AS1411–Cy5. Size, ζ-potential and fluorescent emission were measured to verify GNR-aptamer conjugation (see Table 1 and Fig. 3). Spectrofluorometric data indicate that the concentration of GNRs is consistently reduced during the bioconjugation leading to a reaction yield of 4% in optimized condition. Such loss of GNRs can be probably attributed to extraction of gold atoms to form smaller clusters during the synthesis. H_2N–AS1411–Cy5 conjugation efficiency was approximately estimated by comparing the fluorescence intensity of Cy5 in the supernatant collected after the centrifugation and in AC-GNRs after purification by dialysis. These measurements, conducted in the same conditions, revealed that *ca.* 1.4% of H_2N–AS1411–Cy5 molecules had reacted with GNRs. Taking into account the copious loss of GNRs due to stabilization problems and the large excess of aptamer units applied in this reaction, our findings indicate that H_2N–AS1411–

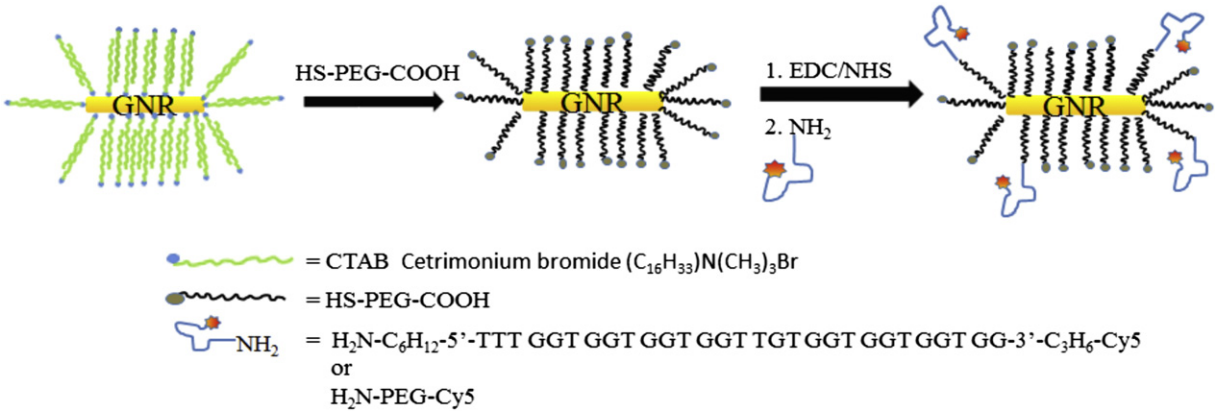

Scheme 1. Schematic representation of the bioconjugation strategy for the synthesis of fluorescent, aptamer-conjugated GNRs.

Table 1
Hydrodynamic diameter and ζ-potential values of GNRs' equivalent spheres measured by dynamic light scattering and NanoSight measurements[a]. Before purification *via* dialysis[b].

GNRs' functionalization	Diameter [nm]	ζ-Potential [mV]
CTAB-GNRs	44; 54[a]	+40
COOH–PEG–GNRs	51[b]; 35	−14[b]; −24
AC-GNRs	47	−35
Cy5–PEG–GNR	51	−9

Cy5 detains a conjugation efficiency closed to unity, that is approximately an average of 10^4 aptamer units per GNR.

2.4. Characterization of GNRs' physical properties

Optical density profiles were measured with a Lambda 25 UV–Vis spectrophotometer (Perkin Elmer, USA), fluorescence spectra were collected using a Fluorolog-3 478 fluorometer (HORIBA JobinYvon, USA). Estimates of the hydrodynamic diameter and ζ-potential of equivalent spheres diffusing in the solution were obtained using a Zetasizer Nano ZS90 dynamic light scattering (DLS) system (Malvern Instruments Ltd., UK). GNRs' hydrodynamic diameter, together with the concentration, was also measured by nanoparticle tracking analysis using a NanoSight LM10 (NanoSight Ltd., UK) placed on a far-field microscope. In these measurements, a diluted solution of GNRs was placed inside of a chamber and irradiated by a He–Ne laser 633 nm beam. Brownian motions of single nanoparticles were recorded over time, tracked and analysed by NanoSight NTA 2.2 Nanoparticle Tracking Analysis software. Each measurement has been repeated three times to ensure reproducibility.

Accurate particle size and AR were determined by transmission electron microscopy (TEM). TEM samples were prepared placing a small drop (8 μl) of diluted GNRs aqueous solution onto a holey carbon film on 300 mesh copper grids and allowing it to evaporate at room temperature. TEM images were acquired using a JEOL 2010 high-resolution transmission electron microscope at an acceleration voltage of 200 kV. The width and length of examined GNRs were evaluated manually using ImageJ. The minimum number of nanoparticles measured was 150 for each sample. The same data were also analysed by a MatLab programme. This routine used the gradient and watershed of TEM images to identify objects, and then measured their length and width. Objects identified as noise are rejected assuming that only elliptical objects should be found. The two analyses gave analogous results. A comparison of the manual and automatic measurements is seen in the supporting information S3 and S4, full details of the programme can be found at https://autoscaleit.wordpress.com/.

2.5. Cell culture and labelling

Human cervical cancer cells HeLa and human oesophageal epithelial cells Het-1A were grown in DMEM supplemented with 10% foetal bovine serum and 1% penicillin–streptomycin (5000 units/mL penicillin G, 50 μg/ml streptomycin sulphate in 0.85% NaCl) at 37 °C with 5% CO_2 humidified atmosphere. Cells were precultured in T-75 flasks and allowed to grow for 5–7 days prior to experiments until 80% confluence was reached. To prepare cell suspensions, adherent cells were quickly rinsed with PBS and then incubated in 5 ml trypsin-EDTA solution (0.25% w/v trypsin, 0.25 g/l EDTA) at 37 °C for 5 min. The cell suspension was then centrifuged at 4500 rpm for 5 min to precipitate the cells to the bottom of the tube. After discarding the upper media, cells were rinsed and re-suspended in 5 ml of culture media. Approximately 10^4 cells were split onto a glass-bottomed culture dishes or 48 well plates and allowed to grow for 12 h before labelling. The day after, cells were washed with 500 μl of PBS and incubated with 200 μl of 0.1 nM solution of GNRs or H_2N–AS1411–Cy5 10 μM dissolved in 2% DMEM at 37 °C with 5% CO_2 humidified atmosphere. After 4 h, cells were rinsed twice with PBS to remove any non-specifically bound GNRs on the cell surface, and were imaged live immerged in red phenol free media. The labelling conditions are based on the protocol reported by Yang et al. [38]. Viability tests were conducted after GNRs' cellular uptake was confirmed by fluorescence imaging. Cells, placed in 48 well plates, were washed with 500 μl of PBS and incubated for 20 min in 500 μl of a freshly prepared of Calcein AM solution (1 μM) prior to fluorescence imaging. The percentage of live cells was estimated comparing the number of cells stained by Calcein AM with the total number of cells appearing in the bright field image within the same field of view. Cell counting was performed using an open source plugin for ImageJ [37].

In flow cytometry measurements, HeLa cells were incubated with AC-GNRs for 20 min before washing. Experiments were performed on fresh samples with 10^6 cells/0.5 mL. The flow cytometer CyAn ADP Analyser (Beckman Coulter, Pasadena, CA U.S.A.) was used: cells flowing in the detection chamber were hit with a 642 nm laser beam, side- and forward-scattered light and fluorescence emission were collected. The latter was filtered by 680/30 band pass filters. All signals were detected by PMT arrays. Representative populations of cells were chosen by selection of an appropriate gate. Detection of cell fluorescence was continued until at least 10^4 events had been collected in the active gate.

2.6. Cell imaging

Cells were imaged on an Olympus IX71 far-field microscope (Olympus, Japan). A 60× oil-immersion objective (Olympus Uplansapo, NA = 1.35) coupled with 1.6× camera coupling lens and a 20× objective (Olympus Uplansapo, NA = 0.75) were used. Bright field and fluorescence images were obtained using a halogen light lamp (Olympus TH4-200), and Lumen 200 metal arc lamp (Prior Scientific Inc., USA), respectively. All images were recorded using a Peltier-cooled CCD camera (Olympus DP30BW) and analysed using ImageJ [37].

3. Results and discussion

3.1. Synthesis and ageing of GNRs produced via seed-mediated growth

GNRs were synthesized through a slightly modified version of the methodology established by Murphy and co-workers [22]. In our procedure, the agitation was constant, while the temperature was kept at 30 °C at each step to guarantee the complete solubilization of CTAB. The duration of the synthesis of seeds and GNRs was determined by verifying that no appreciable change of optical density (OD) profiles occurred at longer times. Additionally, the growth solution was kept in the dark to avoid light induced phenomena. Surprisingly, these small variations led to a significant improvement of the reproducibility. OD profiles of GNRs produced with different amount of $AgNO_3$ are reported in Fig. 1a. It can be noticed that the LSPR maximum shifts towards higher wavelengths with increasing the concentration of silver ions, as a consequence of the modification of GNRs' AR. This result was confirmed by TEM images of GNRs synthesized using different amounts of $AgNO_3$, reported in Fig. 2. This trend is fundamental to establish the optimal conditions for the fabrication of GNRs with specific AR and can help clarifying the specific role of $AgNO_3$ in the growth of GNRs. Fig. 1b depicts a sharp increase of the LSPR peak wavelength (and so of the AR) with the concentration of silver ions up to a threshold value of *ca.* 140 μl of $AgNO_3$ 0.01 M; at higher concentrations this tendency is inverted, probably owing to the interactions between GNRs and the bromide counterions of the surfactant monomers [21]. A plateau is finally reached at *ca.* 200 μl, where variations in the amount of $AgNO_3$ no longer correspond to significant AR changes. Trends reported in previous investigations [39,21] do not show consistency of the positions of the LSPR, testifying the high unpredictability of this synthesis. Interestingly, the presence of a plateau, indicating that the concentration of silver ions reached the saturation limit, is observed here for the first time. $AgNO_3$ is

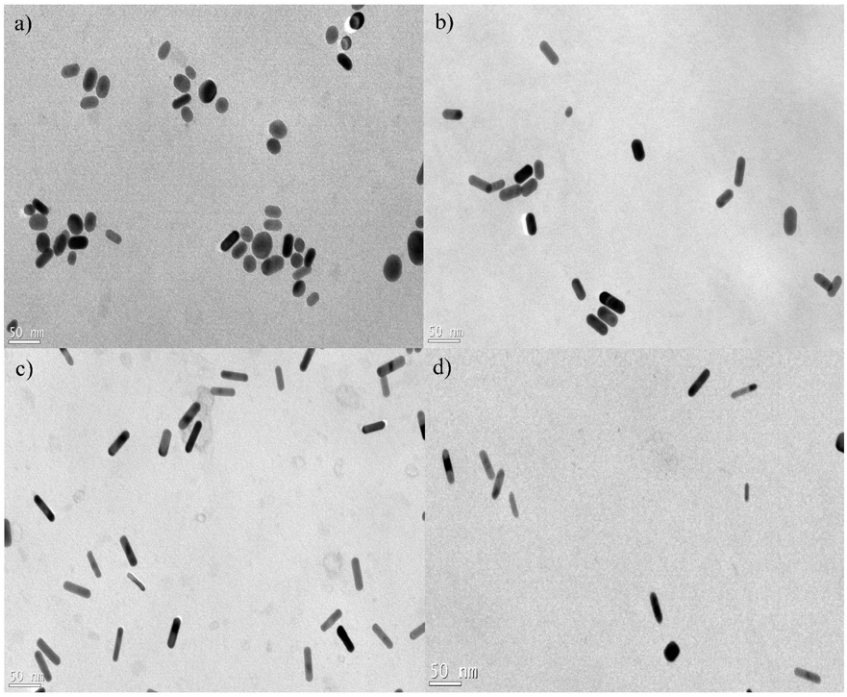

Fig. 2. TEM images of CTAB-coated GNRs produced using different aliquots of $AgNO_3$ 0.01 M and aged for 5 days: 10 μl (a), 25 μl (b), 50 μl (c) and 130 μl (d).

a light-sensitive chemical subject to quick degradation, therefore its effective concentration in the synthetic mixture is in general difficult to obtain. This is a major cause of variability in the fabrication of GNRs with specific AR. In this study, we identified a saturation threshold in $AgNO_3$ concentration, past which the AR of GNRs is constant. This finding overcomes the need of an accurate control when GNRs with AR = 3.9 (LSPR = 795 nm) [40] are needed and can be of practical utility in the synthetic procedure. The repeatability of our method can be evaluated by comparing LSPR positions of GNRs obtained for specific amounts of $AgNO_3$ in different experiments (see Fig. 1b). We believe that the good reproducibility of the synthesis is tied to the application of accurate temperature control. It was previously demonstrated that a complex formed between CTAB, silver, and bromide ions ($C_{19}H_{42}$–$NAgBr_2$) acts as soft template, driving the anisotropic growth of nanoparticles towards the rod shape and influencing their final AR [41,22]. In this respect, the complete solubilization of CTAB at 30°C helps to stabilize the capping complex and its micellar configuration.

In order to detect and characterize ageing phenomena, we monitored spectrophotometric changes of GNRs' solutions obtained with different amounts of $AgNO_3$ as a function of time after the synthesis. It was found that, when CTAB was partially removed by filtration or centrifugation, the LSPR band changed over time presenting a blue shift associated with a slight increase of the OD, as shown in Fig. 1b and S1 of the Supporting Information (SI). No changes were observed when GNRs were kept in the mother solution with native CTAB concentration. Recently, analogous spectrophotometric changes following the synthesis have been reported by da Silva [23]. Interestingly, the authors observed such variations when CTAB was not removed from the GNRs' solution. These changes, which find no correspondence in our study, were explained as a consequence of Ostwald ripening. To assess the origin of the ageing process, we performed TEM measurements on GNRs' solutions produced with 100 (see insets in Fig. 1c and d) and 160 μl of $AgNO_3$ immediately after the synthesis and CTAB removal (day 0), and 5 days later. The analysis of TEM data, conducted both manually than using a MatLab routine (see Fig. S3 in SI), indicate that the average length of GNRs decreased from day 0 to day 5 in both solutions (Fig. 1c and d), while the width changed only in GNRs synthesized with 160 μl of $AgNO_3$, showing an average increase of 0.9 nm. These results prove that the AR varied after the synthesis (from 3.9 (±0.1) to 3.1 (±0.1) for 100 μl of $AgNO_3$ and from 4.0 (±0.1) to 3.4 (±0.1) for 160 μl), however they are not consistent with the occurrence of Ostwald ripening. This phenomenon is generally accompanied by an increase of the volume and by narrowing of the size distribution, while none of these effects was observed in our study. In fact, it is our opinion that the length reduction is related to the destabilization of the rods' ends caused by partial CTAB removal, which in turn leads to a re-equilibrium towards thermodynamically favoured structures. Molecular dynamics calculations suggest that the energetics of the surface facets govern GNRs' stability against shape changes, tending to favour shorter structures [42]. Analogously, a recent study asserted that the surface diffusion of gold atoms is responsible for GNRs reshaping and that this phenomenon, being dependent on the curvature of GNRs, can occur at temperatures far below the bulk melting point [43]. Our results are also compatible with the so called "relaxation stage" of GNRs' growth mechanism reported by Park and co-workers [44], where the rearrangement of the caps to hemispherical shapes provokes shortening of the length.

3.2. Evaluation of the extinction coefficient

The extinction coefficient is a fundamental parameter that defines the suitability for applications requiring light scattering and absorption. Knowledge of this property is also necessary to allow facile and reliable measurement of GNRs' concentration in solutions by simple spectrophotometric measurements. Theoretical studies predict that the extinction coefficient of GNRs is orders of magnitude higher than in organic dyes [45], but, unfortunately, its experimental measurement is not a trivial task. The variability of nanoparticle dimensions, the distribution of their shape and size, and the presence of side products with undesirable shape strongly impact the feasibility of this determination. Nonetheless, performing an independent measurement of GNRs' concentration is challenging itself, due to the high variability of the fabrication yield and to the need of relating the average number of gold atoms present in one nanoparticle to the distribution of shapes and ARs. In previous studies, the concentration of GNRs in solutions of known OD was calculated on the basis of the gold atoms' content measured by

inductively coupled plasma atomic emission spectroscopy (ICP-AES) [46,47]. Extinction coefficients of GNRs were then obtained applying the Lambert–Beer law. In this work, for the first time, the concentration of GNRs with AR = 3.9 was obtained by direct determination via NanoSight analysis, a quick and simple technique with high degree of accuracy. The corresponding extinction coefficient at 795 nm (the maximum of LSPR band) was determined by performing contemporary spectrophotometric analysis on six solutions of different concentrations and calculated from linear fitting analysis ($R^2 = 0.987$, N = 6) of the results. We found that $\varepsilon_{795nm} = 6.3\ 10^9\ (\pm 0.3)\ M^{-1}\ cm^{-1}$; this value is comparable with those obtained by Murphy [47] using ICP-AES ($\varepsilon_{max} = 4.6\ 10^9\ (\pm 0.6)\ M^{-1}\ cm^{-1}$ for GNRs with LSPR centred at 785 nm) and by Hafner [48], who evaluated the extinction coefficient in polyethylene glycol-modified GNRs films.

3.3. Surface functionalization and bioconjugation

Our strategy for the functionalization of GNRs was based on the replacement of CTAB with carboxyl thiol PEG (Scheme 1), exploiting the strong affinity between GNRs and thiols. These groups bind covalently to the gold atoms placed at the surface of the nanoparticles, hence, unlike physical adsorption, this method allows permanent binding of PEG and functional groups to the GNRs. The use of this heterobifunctional polymer includes other advantages linked to the hydrophilic chains, which ensure good solubility in the aqueous phase and constitute a biocompatible shell minimizing non-specific absorption. This shell also forms a steric obstacle to prevent GNRs' aggregation, whereas the negatively charged terminal carboxyl groups further stabilize the colloidal dispersion and constitute reactive functional groups useful for the conjugation with biomolecules following established cross-linking procedures. Despite the superior properties of carboxyl thiol PEG, the formation of aggregates during the ligand exchange procedure was still a possibility. This undesirable phenomenon was addressed by adding a large excess of the polymer with respect to the number of PEG chains expected to ensure full coverage of the particles' surface [36]. Dynamic light scattering size measurements, ζ-potential and OD profiles determinations were done at every step of the procedure to monitor the extent of ligand substitution and nanoparticles' aggregation (see Table 1 and Fig. S2). As shown by the decrease of ζ-potential from positive to negative values, incubation with carboxyl thiol PEG resulted in effective substitution of CTAB. Accordingly, the small variation in the hydrodynamic diameter (see Table 1) and the absence of plasmon coupling in OD profiles proved that aggregation had not occurred. However, absolute ζ values lower than 20 mV indicate that the electrostatic repulsion between the nanoparticles is low. Not surprisingly, extensive aggregation of COOH–PEG–GNRs was observed after one week. We hypothesised that residues of desorbed CTAB had formed complexes with the terminal carboxyl groups of PEG chains, inducing the aggregation of functionalized GNRs. We then decided to perform further purification by dialysis. Dialyzed GNRs displayed a reduction of the hydrodynamic diameter, probably due to different interactions of CTAB-free GNRs' surface with the solvent, and more negative ζ-potential values (see Table 1). Consistently, the change of dielectric constant experienced by the nanoparticles was accompanied by a further shift of 12 nm in the LSPR band (see Fig. S2). PBS solutions of dialyzed COOH–PEG–GNRs were found stable after several months and could be used for the bioconjugation.

Multifunctional GNRs were designed through conjugation of COOH–PEG–GNRs to a fluorescent version of aptamer AS1411 (Scheme 1). AS1411 is constituted by a 26-base guanine-rich oligonucleotide with an unmodified (phosphodiester) DNA backbone. In our strategy, AS1411 was decorated with the fluorophore unit Cy5 on the 3′ end, and with a six carbons spacer followed by an amine group on the 5′ end (H_2N–AS1411–Cy5, see Scheme 1). This approach exploited the modularity of this aptamer to provide GNRs with both cancer-specificity and luminescence, while quenching of the fluorescence emission by GNRs could be excluded on the basis of the long distance between the gold surface and Cy5 units. Conjugation to COOH–PEG–GNRs was obtained through carboxyl-amine cross-linking via EDC/NHS chemistry. Choi and co-workers recently applied an analogous conjugation strategy to produce non-fluorescent GNRs functionalized with anti-epidermal growth factor receptor (EGFR) aptamer [49]. Once the conditions of the reaction were optimized, the same approach was applied to functionalize COOH–PEG–GNRs with Cy5 amine PEG (Cy5–PEG–NH_2). Aptamer conjugated GNRs (AC-GNRs) were then purified through dialysis to eliminate residual unreacted H_2N–AS1411–Cy5 (or Cy5–PEG–NH_2) and examined by spectrophotometric analysis and dynamic light scattering. The comparison of OD profiles of COOH–PEG–GNRs and AC-GNRs, reported in Fig. 3a, pointed out the blue-shift of the LSPR band in AC-GNRs, which could be attributed, once again, to the variation of the dielectric constant. More importantly, the absence of plasmon coupling indicated lack of aggregates, proving that the bioconjugation did not alter the quality of GNRs. This result was confirmed by the value of the hydrodynamic diameter (Table 1), showing elongation due to the cross-linking. ζ-potential values also reflected the effect of conjugation: ζ was reduced in AC-GNRs with respect to COOH–PEG–GNRs, owing to the presence of negatively charged DNA strands, while it increased in Cy5–PEG–GNRs, where part of the carboxyl groups have been employed to bind neutral ligands. Conclusive evidence of the conjugation was given by the characteristic Cy5 emission and excitation profiles observed in dialyzed AC-GNRs water solution (see Fig. 3b). AC-GNRs were stable for several weeks when kept in the dark at 4 °C.

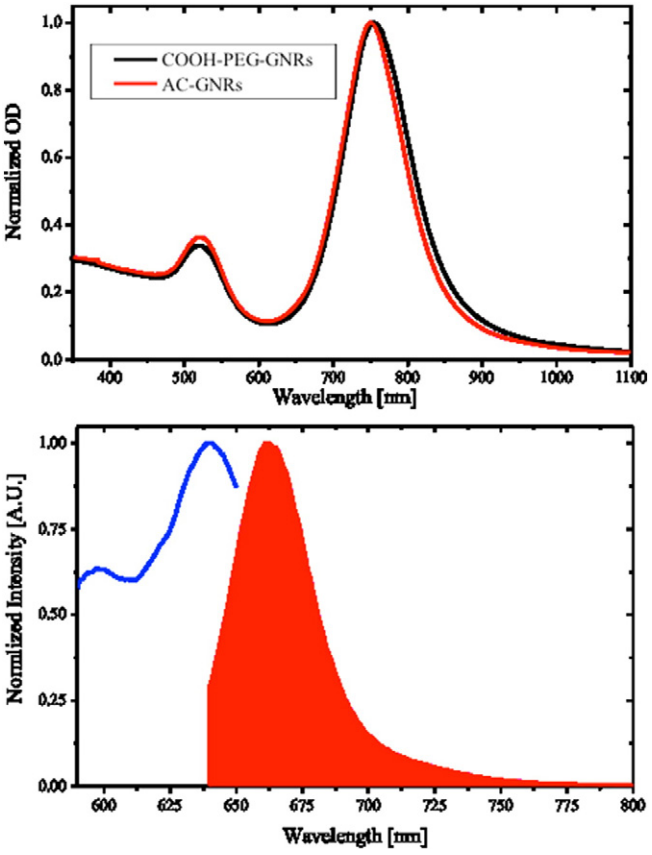

Fig. 3. a) Normalized optical density profiles of COOH–PEG–GNRs in PBS (black line) before and after (red line) bioconjugation to our modified version of aptamer AS1411. b) Fluorescent emission ($\lambda_{exc} = 625$ nm) of AC-GNRs in water solution after purification from unreacted fluorescent aptamer and corresponding excitation spectrum ($\lambda_{em} = 660$ nm).

3.4. Specific targeting of AC-GNRs towards cancer cells

Initially, we verified that our modified, fluorescent version of AS1411 could be internalized by cancer cells via endocytosis. HeLa cells, our cancer model, were incubated with H_2N–AS1411–Cy5 and imaged live through far-field fluorescence microscopy (FFM). Representative bright field, FFM images and corresponding superposition are reported in Fig. 4a–c. Cy5 fluorescent emission from HeLa cells proved that AS1411 affinity to nucleolin was not compromised by the functionalization of 3′- and 5′-ends. In addition, we successfully demonstrated that fluorescent AC-GNRs were uptaken by HeLa cells (see Fig. 4d–f). To corroborate this statement, we also performed flow cytometry experiments on HeLa cells incubated with AC-GNRs. Comparison of fluorescence intensity distributions with untreated cells is reported in Fig. 5a. In order to exclude the possibility that AC-GNRs' internalization could be due to non-specific interactions, we incubated HeLa cells in identical conditions with fluorescent GNRs not provided with any active targeting agent: Cy5–PEG–GNRs. The negligible fluorescence signal reported in Fig. 4i confirmed that the uptake of AC-GNRs is an aptamer-mediated process. These findings establish that the activity of AS1411 was not impaired by the heavy cargo constituted by GNRs, and that non-specific absorption was effectively prevented in PEG-functionalized GNRs. Finally, control of the selectivity of AC-GNRs towards cancer cells was effectuated by applying the labelling procedure on human normal cells Het-1A. Obtained results shown that AC-GNRs were not uptaken by Het-1A cells (see Fig. 4j–l) and confirmed the cancer specificity of AC-GNRs' internalization mechanism. On the basis of these results, we infer that AC-GNRs can be used as cancer-specific multifunctional probes. Indeed, besides the fluorescence signal from Cy5 units, AC-GNRs can also be detected exploiting GNRs' optical properties, for example using dark field microscopy [50], two-photon luminescence [51], photoacoustic imaging [6], or surface enhanced Raman scattering [52]. In order to verify AC-GNRs suitability as multifunctional probes for biological imaging, we tested their cytotoxicity at twice the concentration and after the same incubation time used for fluorescence labelling. We conducted a viability study on HeLa cells via Calcein AM assay, whose results are reported in Fig. 5b. This analysis pointed out that cells incubated for 4 h in 2% DMEM, the solution used for the labelling procedure, displayed reduced viability with respect to cells left in complete DMEM, owing to the low amount of nutrients. However, no toxicity effects due to the incubation with H_2N–AS1411–Cy5, Cy5–PEG–GNRs and AC-GNRs were observed. The absence of toxicity effects against cancer cells by AS1411 can probably be explained considering that, after 4 h of incubation, our labels have not reached the nuclear region yet [53] where the arrest of DNA repair processes and the destabilization of bcl-2 mRNA occur. We predict that migration towards the nucleus could be expedite by increasing the loading density of AS1411 on GNRs, analogously to recent findings on overloaded AS1411-gold nanostars conjugates [54].

In summary, *in vitro* studies corroborate the potential of AC-GNRs as biocompatible, selective probes for cancer detection and possibly treatment based on PTT, thanks to the delivery of the therapeutic cargo

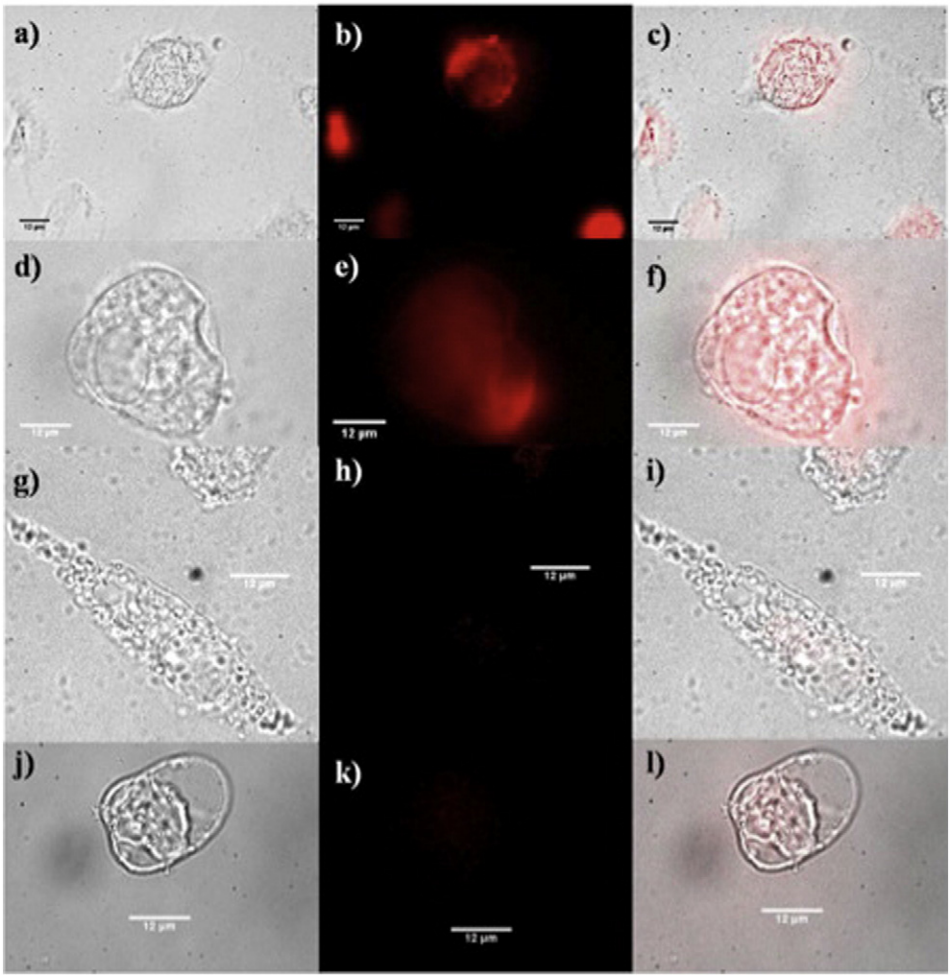

Fig. 4. From left to right: representative bright field, FFM images and their superposition of HeLa cells incubated with H_2N–AS1411–Cy5 (a–c) AC-GNRs (d–f), Cy5–PEG–GNRs (g–i) and HeT-1A cells incubated with AC-GNRs (j–l). Scale bar = 12.0 μm.

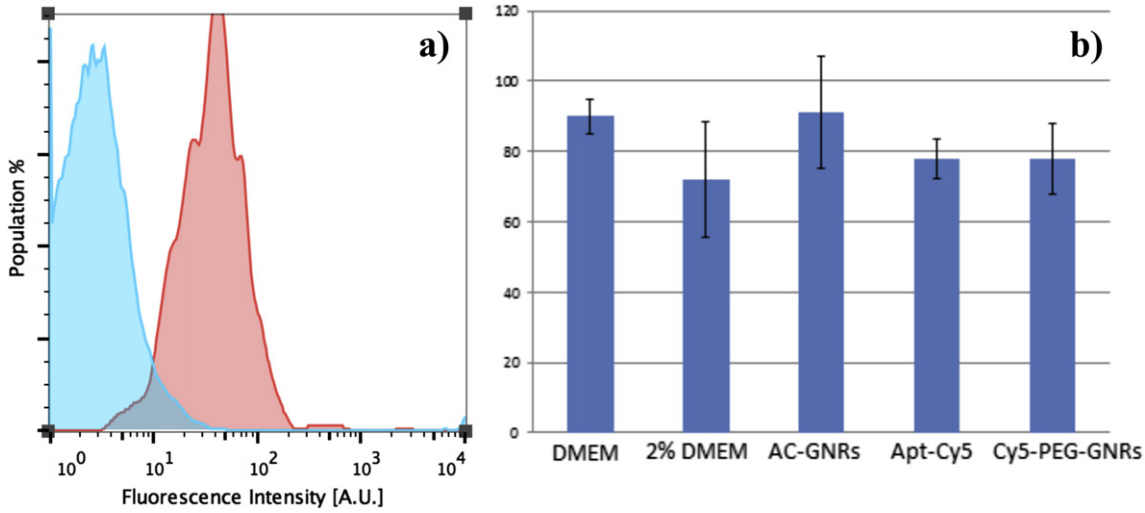

Fig. 5. (a) Flow cytometry fluorescence intensity distributions of HeLa cells incubated with (red curve) and without (light blue curve) AC-GNRs. (b) Viability study on HeLa cells *via* Calcein AM assay. From left to right: percentage of live cells after 4 h of incubation with complete DMEM (positive control), 2% DMEM, 0.2 nM AC-GNRs, 10 μM H_2N–AS1411–Cy5 (Apt-Cy5) and 0.2 nM Cy5–PEG–GNRs in 2% DMEM.

inside of the cytosol of cancer cells. This cancer-treatment application is currently under investigations by our group and will be the object of a future work.

4. Conclusion

In this work, we presented developments on the seed-mediated fabrication of GNRs and on the characterization of obtained CTAB-coated GNRs. Secondly, we extensively modified the native surface functionalization of GNRs to provide multifunctional cancer selective nanoconstructs. *In vitro* studies confirmed the biocompatibility and high specificity of our nanoprobes.

Specifically, the fabrication method of GNRs [22] was refined to providing a robust and reproducible procedure, which showed a new dependence of LSPR position (and GNRs' AR) on the amount of $AgNO_3$. This result detains practical utility in the synthesis practise of GNRs with AR = 3.9, but it also helps to clarify the role of $AgNO_3$ in the mechanism of GNRs' formation. We also brought to light the occurrence of aging phenomena that follow the GNRs' most common synthetic method and significantly alter their optical properties in the NIR. Changes of the OD profiles have been attributed to mutations of GNRs' structure revealed by TEM measurements. Possible explanations have been found in the destabilization of GNRs' caps due to the partial removal of the surfactant, followed by reorganization towards thermodynamically favoured, shorter structures. Further characterization of GNRs with AR = 3.9 has been done with the determination of the extinction coefficient at the LSPR maximum, obtained for the first time using optical concentration measurements based on nanoparticles tracking.

CTAB-coated GNRs were successfully modified to obtain non-toxic, multifunctional nanosystems. Good biocompatibility and stability in water solutions were achieved by exchanging CTAB double-layer with PEG chains. Bioconjugation with a fluorescent, active targeting agent, H_2N–AS1411–Cy5, was secured using a versatile cross-linking method based on the exploitation of aptamers' modularity. Flow cytometry experiments and FFM studies evidenced the efficiency of AC-GNRs' uptake by cancer cells. We also demonstrated that it is a cancer selective, aptamer-mediated process, while GNRs' absorption due to non-specific interactions is negligible. These nanoconstructs have also been proved not to exert cytotoxic effects at double concentrations with respect to the amount needed for detection via fluorescence microscopy. These findings allowed us to classify AC-GNRs as promising cancer-selective, multifunctional probes. AC-GNRs also represent good candidates for theradiagnostic applications based on the use of PTT, this possible application is currently under investigations and will be presented in a future work.

Conflicts of interests

All authors declare that they have no conflicts of interests.

Acknowledgements

We gratefully acknowledge the donation of HeLa and HeT-1A cells from Molly Stevens' group of Imperial College London and the assistance provided by Dr. Manuel M Mazo and Dr. Ciro Chiappini. Funding for this project was provided by the ERC grant StG242991.

Appendix A. Supplementary data

Supplementary data to this article can be found online at http://dx.doi.org/10.1016/j.msec.2015.09.101.

References

[1] L.C. Kennedy, L.R. Bickford, N.A. Lewinski, A.J. Coughlin, Y. Hu, E.S. Day, et al., A new era for cancer treatment: gold-nanoparticle-mediated thermal therapies, Small 7 (2011) 169–183.
[2] C. Burda, X. Chen, R. Narayanan, M.A. El-Sayed, Chemistry and properties of nanocrystals of different shapes, Chem. Rev. 105 (2005) 1025–1102, http://dx.doi.org/10.1021/cr030063a.
[3] H. Wang, T.B. Huff, D.A. Zweifel, W. He, P.S. Low, A. Wei, et al., In vitro and in vivo two-photon luminescence imaging of single gold nanorods, Proc. Natl. Acad. Sci. U. S. A. 102 (2005) 15752–15756.
[4] N.J. Durr, T. Larson, D.K. Smith, B.A. Korgel, K. Sokolov, A. Ben-Yakar, Two-photon luminescence imaging of cancer cells using molecularly targeted gold nanorods, Nano Lett. 7 (2007) 941–945, http://dx.doi.org/10.1021/nl062962v.
[5] D.C. Adler, S.-W. Huang, R. Huber, Photothermal detection of gold nanoparticles using phase-sensitive optical coherence tomography, Opt. Express 16 (2008) 4376–4393.
[6] A. Agarwal, S.W. Huang, M. O'Donnell, K.C. Day, M. Day, N. Kotov, et al., Targeted gold nanorod contrast agent for prostate cancer detection by photoacoustic imaging, J. Appl. Phys. 102 (2007) 064701, http://dx.doi.org/10.1063/1.2777127.
[7] A. Wei, A.P. Leonov, Q. Wei, Gold Nanorods: Multifunctional Agents for Cancer Imaging and Therapy, in: S.R. Grobmyer, B.M. Moudgil (Eds.), Cancer Nanotechnol.Humana Press, Totowa, NJ 2010, pp. 119–130 (http://www.springerlink.com/index/10.1007/978-1-60761-609-2_8).
[8] A. Kopwitthaya, K.-T. Yong, R. Hu, I. Roy, H. Ding, L.A. Vathy, et al., Biocompatible PEGylated gold nanorods as colored contrast agents for targeted *in vivo* cancer applications, Nanotechnology 21 (2010) 315101, http://dx.doi.org/10.1088/0957-4484/21/31/315101.
[9] Y. Jung, R. Reif, Y. Zeng, R.K. Wang, Three-dimensional high-resolution imaging of gold nanorods uptake in sentinel lymph nodes, Nano Lett. 11 (2011) 2938–2943, http://dx.doi.org/10.1021/nl2014394.

[10] J.A. Schwartz, R.E. Price, K.L. Gill-Sharp, K.L. Sang, J. Khorchani, B.S. Goodwin, et al., Selective nanoparticle-directed ablation of the canine prostate, Lasers Surg. Med. 43 (2011) 213–220, http://dx.doi.org/10.1002/lsm.21039.
[11] J. Wang, G. Zhu, M. You, E. Song, M.I. Shukoor, K. Zhang, et al., Assembly of aptamer switch probes and photosensitizer on gold nanorods for targeted photothermal and photodynamic cancer therapy, ACS Nano 6 (2012) 5070–5077, http://dx.doi.org/10.1021/nn300694v.
[12] R. Chen, X. Zheng, H. Qian, X. Wang, J. Wang, X. Jiang, Combined near-IR photothermal therapy and chemotherapy using gold-nanorod/chitosan hybrid nanospheres to enhance the antitumor effect, Biomater. Sci. 1 (2013) 285, http://dx.doi.org/10.1039/c2bm00138a.
[13] X. Huang, I.H. El-Sayed, W. Qian, M.A. El-Sayed, Cancer cell imaging and photothermal therapy in the near-infrared region by using gold nanorods, J. Am. Chem. Soc. 128 (2006) 2115–2120, http://dx.doi.org/10.1021/ja057254a.
[14] R. Guo, L. Zhang, H. Qian, R. Li, X. Jiang, B. Liu, Multifunctional nanocarriers for cell imaging, drug delivery, and near-IR photothermal therapy, Langmuir 26 (2010) 5428–5434, http://dx.doi.org/10.1021/la903893n.
[15] Y. Zhang, J. Qian, D. Wang, Y. Wang, S. He, Multifunctional gold nanorods with ultrahigh stability and tunability for in vivo fluorescence imaging, SERS detection, and photodynamic therapy, Angew. Chem. Int. Ed. 52 (2013) 1148–1151, http://dx.doi.org/10.1002/anie.201207909.
[16] L. Hirsch, R.J. Stafford, J.A. Bankson, S.R. Sershen, B. Rivera, R.E. Price, et al., Nanoshell-mediated near-infrared thermal therapy of tumors under magnetic resonance guidance, Proc. Natl. Acad. Sci. 100 (2003) 13549–13554.
[17] S. Shen, H. Tang, X. Zhang, J. Ren, Z. Pang, D. Wang, et al., Targeting mesoporous silica-encapsulated gold nanorods for chemo-photothermal therapy with near-infrared radiation, Biomaterials 34 (2013) 3150–3158, http://dx.doi.org/10.1016/j.biomaterials.2013.01.051.
[18] L.B. Carpin, L.R. Bickford, G. Agollah, T.-K. Yu, R. Schiff, Y. Li, et al., Immunoconjugated gold nanoshell-mediated photothermal ablation of trastuzumab-resistant breast cancer cells, Breast Cancer Res. Treat. 125 (2010) 27–34, http://dx.doi.org/10.1007/s10549-010-0811-5.
[19] P.K. Jain, X. Huang, I.H. El-Sayed, M.A. El-Sayed, Noble metals on the nanoscale: optical and photothermal properties and some applications in imaging, sensing, biology, and medicine, Acc. Chem. Res. 41 (2008) 1578–1586, http://dx.doi.org/10.1021/ar7002804.
[20] N.R. Jana, L. Gearheart, C.J. Murphy, Seed-mediated growth approach for shape-controlled synthesis of spheroidal and rod-like gold nanoparticles using a surfactant template, Adv. Mater. 13 (2001) 1389.
[21] B. Nikoobakht, M.A. El-Sayed, Preparation and growth mechanism of gold nanorods (NRs) using seed-mediated growth method, Chem. Mater. 15 (2003) 1957–1962, http://dx.doi.org/10.1021/cm020732l.
[22] J.A. Yang, S.E. Lohse, S.P. Boulos, C.J. Murphy, The early life of gold nanorods: temporal separation of anisotropic and isotropic growth modes, J. Clust. Sci. 23 (2012) 799–809, http://dx.doi.org/10.1007/s10876-012-0474-y.
[23] M.G.A. da Silva, Á.M. Nunes, S.M.P. Meneghetti, M.R. Meneghetti, New aspects of gold nanorod formation via seed-mediated method, C. R. Chim. 16 (2013) 640–650, http://dx.doi.org/10.1016/j.crci.2013.01.013.
[24] E.E. Connor, J. Mwamuka, A. Gole, C.J. Murphy, M.D. Wyatt, Gold nanoparticles are taken up by human cells but do not cause acute cytotoxicity, Small 1 (2005) 325–327, http://dx.doi.org/10.1002/smll.200400093.
[25] B. Thierry, J. Ng, T. Krieg, H.J. Griesser, A robust procedure for the functionalization of gold nanorods and noble metal nanoparticles, Chem. Commun. 1724 (2009)http://dx.doi.org/10.1039/b820137d.
[26] W.M. Park, B.G. Choi, Y.S. Huh, W.H. Hong, S.Y. Lee, T.J. Park, Facile functionalization of colloidal gold nanorods by the specific binding of an engineered protein that is preferred over CTAB bilayers, ChemPlusChem 78 (2013) 48–51, http://dx.doi.org/10.1002/cplu.201200239.
[27] H. Takahashi, Y. Niidome, T. Niidome, K. Kaneko, H. Kawasaki, S. Yamada, Modification of gold nanorods using phosphatidylcholine to reduce cytotoxicity, Langmuir 22 (2006) 2–5, http://dx.doi.org/10.1021/la0520029.
[28] G. Zhang, Z. Yang, W. Lu, R. Zhang, Q. Huang, M. Tian, et al., Influence of anchoring ligands and particle size on the colloidal stability and in vivo biodistribution of polyethylene glycol-coated gold nanoparticles in tumor-xenografted mice, Biomaterials 30 (2009) 1928–1936, http://dx.doi.org/10.1016/j.biomaterials.2008.12.038.
[29] Y. Matsumura, H. Maeda, A new concept for macromolecular therapeutics in cancer chemotherapy: mechanism of tumoritropic accumulation of proteins and the antitumor agent smancs, Cancer Res. 46 (1986) 6387–6392.
[30] P. Tiwari, K. Vig, V. Dennis, S. Singh, Functionalized gold nanoparticles and their biomedical applications, Nanomaterials 1 (2011) 31–63, http://dx.doi.org/10.3390/nano1010031.
[31] R.G. Rayavarapu, W. Petersen, C. Ungureanu, J.N. Post, T.G. van Leeuwen, S. Manohar, Synthesis and bioconjugation of gold nanoparticles as potential molecular probes for light-based imaging techniques, Int. J. Biomed. Imaging 2007 (2007) 1–10, http://dx.doi.org/10.1155/2007/29817.
[32] M. Eghtedari, A.V. Liopo, J.A. Copland, A.A. Oraevsky, M. Motamedi, Engineering of hetero-functional gold nanorods for the in vivo molecular targeting of breast cancer cells, Nano Lett. 9 (2009) 287–291, http://dx.doi.org/10.1021/nl802915q.
[33] X. Fang, W. Tan, Aptamers generated from cell-SELEX for molecular medicine: a chemical biology approach, Acc. Chem. Res. 43 (2010) 48–57, http://dx.doi.org/10.1021/ar900101s.
[34] C.R. Ireson, L.R. Kelland, Discovery and development of anticancer aptamers, Mol. Cancer Ther. 5 (2006) 2957–2962, http://dx.doi.org/10.1158/1535-7163.MCT-06-0172.
[35] S. Soundararajan, L. Wang, V. Sridharan, W. Chen, N. Courtenay-Luck, D. Jones, et al., Plasma membrane nucleolin is a receptor for the anticancer aptamer AS1411 in MV4-11 leukemia cells, Mol. Pharmacol. 76 (2009) 984–991, http://dx.doi.org/10.1124/mol.109.055947.
[36] J. Manson, D. Kumar, B.J. Meenan, D. Dixon, Polyethylene glycol functionalized gold nanoparticles: the influence of capping density on stability in various media, Gold Bull. 44 (2011) 99–105, http://dx.doi.org/10.1007/s13404-011-0015-8.
[37] C.A. Schneider, W.S. Rasband, K.W. Eliceiri, NIH image to ImageJ: 25 years of image analysis, Nat. Methods 9 (2012) 671–675, http://dx.doi.org/10.1038/nmeth.2089.
[38] X. Yang, X. Liu, Z. Liu, F. Pu, J. Ren, X. Qu, Near-infrared light-triggered, targeted drug delivery to cancer cells by aptamer gated nanovehicles, Adv. Mater. 24 (2012) 2890–2895, http://dx.doi.org/10.1002/adma.201104797.
[39] S.S. Seo, X. Wang, D. Murray, Direct monitoring of gold nanorod growth, Ionics 15 (2008) 67–71, http://dx.doi.org/10.1007/s11581-008-0223-2.
[40] S. Link, M.B. Mohamed, M.A. El-Sayed, Simulation of the optical absorption spectra of gold nanorods as a function of their aspect ratio and the effect of the medium dielectric constant, J. Phys. Chem. B 103 (1999) 3073–3077, http://dx.doi.org/10.1021/jp990183f.
[41] J.A. Edgar, A.M. McDonagh, M.B. Cortie, Formation of gold nanorods by a stochastic "popcorn" mechanism, ACS Nano 6 (2012) 1116–1125, http://dx.doi.org/10.1021/nn203586j.
[42] Y. Wang, S. Teitel, C. Dellago, Surface-driven bulk reorganization of gold nanorods, Nano Lett. 5 (2005) 2174–2178, http://dx.doi.org/10.1021/nl051149h.
[43] A.B. Taylor, A.M. Siddiquee, J.W.M. Chon, Below melting point photothermal reshaping of single gold nanorods driven by surface diffusion, ACS Nano 8 (2014) 12071–12079, http://dx.doi.org/10.1021/nn5055283.
[44] K. Park, L.F. Drummy, R.C. Wadams, H. Koerner, D. Nepal, L. Fabris, et al., Growth mechanism of gold nanorods, Chem. Mater. 25 (2013) 555–563, http://dx.doi.org/10.1021/cm303659q.
[45] P.K. Jain, K.S. Lee, I.H. El-Sayed, M.A. El-Sayed, Calculated absorption and scattering properties of gold nanoparticles of different size, shape, and composition: applications in biological imaging and biomedicine, J. Phys. Chem. B 110 (2006) 7238–7248, http://dx.doi.org/10.1021/jp057170o.
[46] B. Nikoobakht, J. Wang, M.A. El-Sayed, Surface-enhanced Raman scattering of molecules adsorbed on gold nanorods: off-surface Plasmon resonance condition, Chem. Phys. Lett. 366 (2002) 17–23.
[47] C.J. Orendorff, C.J. Murphy, Quantitation of metal content in the silver-assisted growth of gold nanorods, J. Phys. Chem. B 110 (2006) 3990–3994, http://dx.doi.org/10.1021/jp0570972.
[48] H. Liao, J.H. Hafner, Gold nanorod bioconjugates, Chem. Mater. 17 (2005) 4636–4641, http://dx.doi.org/10.1021/cm050935k.
[49] J. Choi, Y. Park, E.B. Choi, H.-O. Kim, D.J. Kim, Y. Hong, et al., Aptamer-conjugated gold nanorod for photothermal ablation of epidermal growth factor receptor-overexpressed epithelial cancer, J. Biomed. Opt. 19 (2013)http://dx.doi.org/10.1117/1.JBO.19.5.051203 (051203-051203).
[50] J.W. Stone, P.N. Sisco, E.C. Goldsmith, S.C. Baxter, C.J. Murphy, Using gold nanorods to probe cell-induced collagen deformation, Nano Lett. 7 (2007) 116–119, http://dx.doi.org/10.1021/nl062248d.
[51] L. Tong, Q. Wei, A. Wei, J.-X. Cheng, Gold nanorods as contrast agents for biological imaging: optical properties, surface conjugation and photothermal effects†, Photochem. Photobiol. 85 (2009) 21–32.
[52] G. von Maltzahn, A. Centrone, J.-H. Park, R. Ramanathan, M.J. Sailor, T.A. Hatton, et al., SERS-coded gold nanorods as a multifunctional platform for densely multiplexed near-infrared imaging and photothermal heating, Adv. Mater. 21 (2009) 3175–3180, http://dx.doi.org/10.1002/adma.200803464.
[53] D.H.M. Dam, J.H. Lee, P.N. Sisco, D.T. Co, M. Zhang, M.R. Wasielewski, et al., Direct observation of nanoparticle–cancer cell nucleus interactions, ACS Nano 6 (2012) 3318–3326, http://dx.doi.org/10.1021/nn300296p.
[54] D.H.M. Dam, R.C. Lee, T.W. Odom, Improved in vitro efficacy of gold nanoconstructs by increased loading of G-quadruplex aptamer, Nano Lett. 14 (2014) 2843–2848, http://dx.doi.org/10.1021/nl500844m.